https://doi.org/10.5194/wes-2022-81
Preprint. Discussion started: 14 October 2022

eawe european academy of wind energy
Open Access WIND ENERGY SCIENCE DISCUSSIONS

Towards Smart Blades for Vertical Axis Wind Turbines: Different Airfoil Shapes and Tip Speed Ratios

M. Rasoul Tirandaz[1], Abdolrahim Rezaeiha[2,3], Daniel Micallef[1]

[1] University of Malta, Department of Environmental Design, Msida, MSD2080, Malta
[2] KU Leuven, Leuven, Belgium
[3] Eindhoven University of Technology, Eindhoven, The Netherlands

Correspondence to: M. Rasoul Tirandaz (msctirandaz@gmail.com)

Abstract. Future wind turbines will benefit from state-of-the-art technologies that allow them to not only operate efficiently in any environmental condition, but also to maximize the power output and cut the cost of energy production. Smart technology, based on morphing blades, is one of the promising tools that could make this possible. The present study serves as a basis for identifying morphing airfoils as functions of azimuthal angle and tip speed ratio for vertical axis wind turbines. The focus of this work is on the combined analysis of three airfoil shape-defining parameters, namely the maximum thickness *t/c* and its chordwise position *xt/c* as well as the leading-edge radius index *I*. A total of 126 airfoils are generated. The analysis is based on 630 high-fidelity transient CFD simulations, validated with three experiments. The results show that with increasing λ, the optimal maximum thickness decreases from 24%c to 10%c, its chordwise position shifts from 35%c to 22.5%c, while the corresponding leading-edge radius index remains at 4.5. The results show an average improvement of nearly 0.06 in C_P for all the values of λ.

Keywords. Smart rotor design; Morphing airfoil; Shape adaptation; wind energy; Computational fluid dynamics (CFD).

Nomenclature

α	Angle of attack [°]	k	Reduced frequency, $\Omega c/2V_{ref} \approx c/2R$ [-]
α_{ss}	Static stall angle [°]	L	Lift [N]
θ	Azimuth angle [°]	M	Turbine moment [Nm]
λ	Tip speed ratio, $R\Omega/U_\infty$ [-]	n	Number of blades [-]
ν	Kinematic viscosity of air [m^2/s]	P	Turbine output power [W]
σ	Solidity, nc/d [-]	q	Dynamic pressure [Pa]
Ω	Turbine rotational speed [rad/s]	R	Turbine radius [m]
A	Turbine swept area, $h.d$ [m^2]	Re_c	Chord-based Reynolds number, $cU_\infty\sqrt{1+\lambda^2}/\nu$ [-]
c	Airfoil chord length [m]	r_{LE}	Airfoil leading-edge radius [%c]
C_d	Drag coefficient, D/qA [-]	T	Turbine thrust force [N]
C_f	Skin friction coefficient, D/qA [-]	t/c	Airfoil relative maximum thickness [%]
C_l	Lift coefficient, L/qA [-]	U_∞	Freestream velocity [m/s]
C_m	Moment coefficient, $M/(qAR)$ [-]	U	Instantaneous streamwise velocity [m/s]
C_P	Turbine power coefficient, $P/(qAU_\infty)$ [-]	V	Instantaneous lateral velocity [m/s]
C_T	Turbine thrust coefficient, $T/(qA)$ [-]	$V_{tan,n}$	Dimensionless instantaneous tangential velocity, $(u\cos(\theta)+v\sin(\theta))/U_\infty$ [-]
D	Drag [N]	V_{rel}	Relative velocity [m/s]
h	Turbine height [m]	xt/c	Dimensionless chordwise-position of airfoil maximum thickness [%]
I	Airfoil leading-edge radius index [-]	TI	Turbulence intensity [%]

1. Introduction

1.1 State of the art

Morphing technology has the potential to improve the performance of flying bodies by adapting their shape to different operational conditions. This can result in improved aerodynamic efficiency and the release of unwanted stresses [1, 2]. Nature has given birds

https://doi.org/10.5194/wes-2022-81
Preprint. Discussion started: 14 October 2022

the capability of continuous morphing to generate enough lift for various flight maneuvers. These bio-inspirational sources served as models for possible morphing vehicles and provided the pioneering researchers with a new method of improving aerodynamic efficiency [3]. However, because of the technological limitations of the day, it was not possible to reach the level of smooth shape-changing capabilities as seen in birds. This led to the development of shape-changing by using ailerons, slats, flaps or variable sweep [1]. Nowadays, advances in smart technologies have enabled such needs to be satisfied. Wing morphing is used in the aerospace industry to improve the aerodynamic efficiency and adaptability of aircraft [4-8], helicopters [9-12], micro air vehicles [13-17] and unmanned air vehicles [18-21]. In contrast, the blades of wind turbines operate at relatively low wind speeds with a low level of risk. Nevertheless, morphing technology can still be of benefit for wind turbine purposes without the challenges that must be overcome in aerospace applications (e. g., increasing weight and complexity) [22]. For horizontal axis wind turbines (HAWTs), the impact of morphing blades on load control has been studied by [23-33].

The angle of attack α of a vertical axis wind turbine (VAWT) blade varies periodically between positive and negative values. Through this quasi-sinusoidal variation of α, it exceeds the static stall angle, α_{ss}, and the blade undergoes unsteady separation, resulting in the occurrence of dynamic stall and hysteresis effects on aerodynamic loads [25, 34-37]. When a turbine is operating at low λ, it benefits from the early stages of dynamic stall; that is, the performance of the blade increases due to an overshoot in lift coefficient C_l; however, the overall power output is affected negatively by the consequential sudden drop in C_l [38, 39]. This sophisticated aerodynamics makes the development of a single optimal airfoil for VAWTs a challenging process.

To this date, the performance of VAWTs, which very often use airfoils used in the helicopter industry [40, 41], has been studied for airfoil parameters as proposed in [42-46]. More recently, a few studies have been conducted to improve VAWTs performance via optimizing the airfoil [47-49]. This dependency of VAWT performance on airfoil shape means that the design of morphing blades, which can adapt their shapes to variables such as azimuthal angle θ and λ is worth pursuing. In other words, as the airfoil morphs into a new geometry due to changes in azimuthal position or wind speed, the separation point will move to an optimal coordinate. As a result, flow detachment can be reduced or delayed to higher α, and severe dynamic stall can be controlled or even avoided in the case of unsteady separation at low λ, resulting in improved aerodynamic and power performance [39, 50].

Detailed analysis of the literature shows that the majority of studies focused on morphing trailing edges. For example, experimental [51] and numerical [52] studies show that morphing the trailing edge results in significant power regulation and aerodynamic load reduction. In another work [53] a deformable trailing edge was discovered to improve the power output of VAWTs. [50] showed that morphing aileron improves the aerodynamic performance of VAWTs. In a numerical study, it was found that the airfoil parameters have a substantial impact on the power performance of VAWT operating in the dynamic stall regime [39].

Despite the existence of this reported literature, several shape-defining parameters have received much less attention. Such parameters are hypothesised to have an influence on boundary layer events and the resultant aerodynamic loads. Therefore, a parametric analysis of these variables, with their potential to morph, would provide fundamental knowledge towards designing morphing blades for smart VAWTs.

1.2 Objectives

The present work follows the objectives below:

i. To pave the road towards smart blades for VAWTs, having the capability of adaptation to different operational conditions.
ii. To provide a set of generalizable conclusions from 630 transient simulations for 126 identical airfoils, generated with different values of maximum thickness t/c, chordwise position of maximum thickness xt/c, and leading-edge radius index I at 5 different tip speed ratios λ; and thus, understand the impact of different morphing blade scenarios on the turbine power performance C_P as well as the thrust performance C_T.

https://doi.org/10.5194/wes-2022-81
Preprint. Discussion started: 14 October 2022

The reference airfoil is chosen from the symmetric modified NACA four-digit series. The morphing airfoils are generated through changing the combination of the three aforementioned parameters. An unsteady Reynolds-Averaged Navier-Stokes (URANS) approach, validated with experimental data, will be used for the analysis. The results will provide a set of optimal airfoils at each λ, as well as each azimuth angle, and thus, making a conceptual step towards designing morphing blades for VAWTs.

1.3 Paper outline

The paper is organized as follows: Sect. 2 presents the computational settings and parameters for the simulations. The solution verification and validation studies are also included. Sect. 3 introduces the generated airfoil shapes. In Sect. 4, the results are presented in two scenarios. Sect. 5 and 6 are devoted to the discussion and conclusions.

2. Computational settings and parameters

2.1 Reference turbine characteristics

A single-bladed Darrieus H-type VAWT was chosen as the reference case for this study (see Table 1 and Fig. 1). The turbine is a simplified representation of the original one used by [54]. That is, the turbine shaft and spokes are removed, and there is only one blade. Note that the conclusions are not significantly affected by these components. The reader is referred to our earlier works [55, 56] where it is shown that for low solidity VAWTs, the power performance is almost independent of the shaft and number of blades. Therefore, such a simplified turbine model can effectively reduce the computational costs of the huge number of simulations (i. e., 630 transient simulations) for the present work and, at the same time, provide reliable results. Refs. [56, 57] are used to select the rest of the geometrical and operational characteristics of the reference turbine.

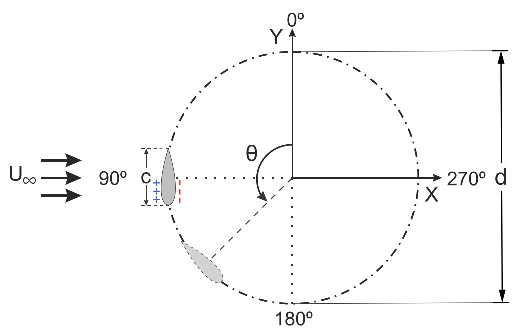

Figure 1: The reference turbine (not to scale). (+): airfoil pressure side and (-): suction side for $0° \leq \theta < 180°$.

Table 1: Characteristics of the reference turbine.

Turbine type	Darrieus H-type
N	1
D	1 m
σ	0.06
Airfoil shape	NACA0018-6.0/3.0 (i.e., baseline NACA0018) t/c = 18%; I = 6.0; xt/c = 30%
Blade/Spoke connection point	c/2
U_∞	9.3 m/s
Λ	2.5, 3.0, 3.5, 4.5, 5.0
Ω	46.5, 55.8, 65.1, 83.7, 93.0 rad/s
C	0.06 m
Re_c [$\times 10^5$]	1.03, 1.20, 1,40, 1.76, 1.95
TI	5%

2.2 Computational settings

https://doi.org/10.5194/wes-2022-81
Preprint. Discussion started: 14 October 2022

WIND ENERGY SCIENCE DISCUSSIONS

The commercial flow solver ANSYS Fluent v2019R2 is employed for the 2D incompressible URANS simulations coupled with the four-equation transition SST turbulence model. The simulations are solved using second-order spatial/temporal discretization and the SIMPLE pressure-velocity coupling scheme. The computational domain, grid, and boundary conditions are summarized in Table 2. The schematic of the computational domain and the computational grid and its subregions are shown in Fig.2.

The turbulence model is selected based on our previous findings [58-60]. Best-practice guidelines for the CFD simulations of VAWTs are used to select the domain size, the azimuthal increment, and the convergence criterion [61]. The corresponding absolute time-step values are 3.75339546×10^{-5} s, 3.12782955×10^{-5} s, 2.68099676×10^{-5} s, 2.0852197×10^{-5} s and 1.70608885×10^{-5} s for $\lambda = 2.5$, 3.0, 3.5, 4.5 and 5.5, respectively. With the selected $d\theta = 0.1$, 3600 time-steps per turbine revolution are achieved. A total number of 20 revolutions, i.e., 72,000 time-steps, are simulated before the results of the present study are obtained at the 21st turbine revolution. Under these conditions, the statistical convergence of the transient simulations is ensured. In each case, a number of 20 iterations per time-step is performed so that the scaled residuals stay $< 10^{-5}$.

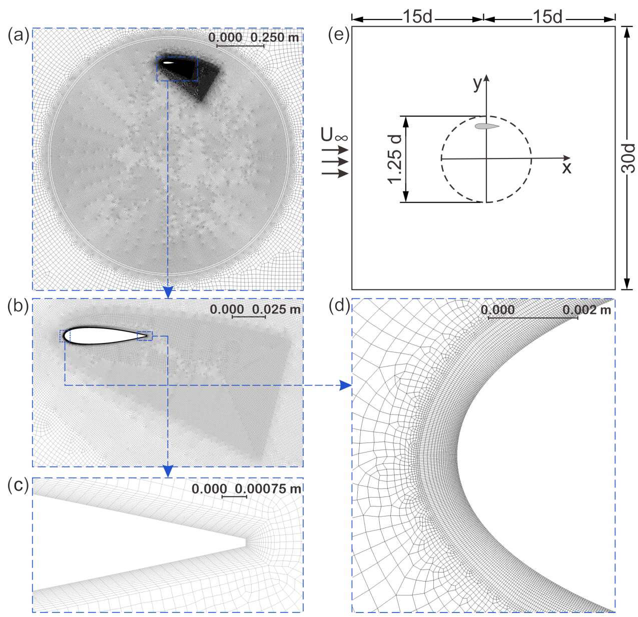

Figure 2. (a-d) the grid; and (e) schematic of the computational domain (not to scale).

Table 2: Details of computational domain, grid, and boundary conditions.

Computational domain (see Fig. 2e)	30d × 30d (d: turbine diameter)
Computational grid (see Fig. 2a-d)	*Cell type*: quadrilateral *Cell No.*: 302,815 *No. of cells around the airfoil circumference*: 800 $y^+_{max} < 2.5$
Boundary conditions	*Inlet*: uniform normal velocity (Turbulence length scale = d); *Outlet*: zero static gauge pressure;

2.3 Solution verification and validation

The domain type is selected based on our earlier studies, where the difference between 2D and 2.5D URANS simulations was found to be insignificant [57]. A grid convergence analysis using uniformly-doubled grids has been performed and documented in Ref. [62], which for brevity is not repeated here. Three experimental studies with different test conditions are used to validate the CFD simulations. The different geometrical and operational characteristics of the turbines used in the experiments led to dissimilar

https://doi.org/10.5194/wes-2022-81
Preprint. Discussion started: 14 October 2022

conclusions [25, 54, 63], ensuring a high level of confidence in the accuracy of the CFD simulations. However, the reader is referred to Ref. [59] for more detailed descriptions of the validation studies.

3. Morphing airfoil shapes

Figure 3 shows a schematic drawing of the symmetric modified NACA 4-digit airfoil and the selected shape-defining parameters for this study. These parameters are morphed within their most common regimes as follows:

(i) relative maximum thickness (*t/c*): 10, 12, 15, 18, 21 and 24%;
(ii) relative chordwise position of maximum thickness (*xt/c*): 20, 22.4, 25, 27.5, 30, 35 and 40%;
(iii) index of leading-edge radius (*I*): 4.5, 6.0 and 7.5.

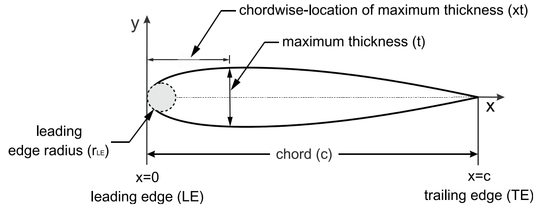

Figure 3: Defining parameters of the symmetric airfoil.

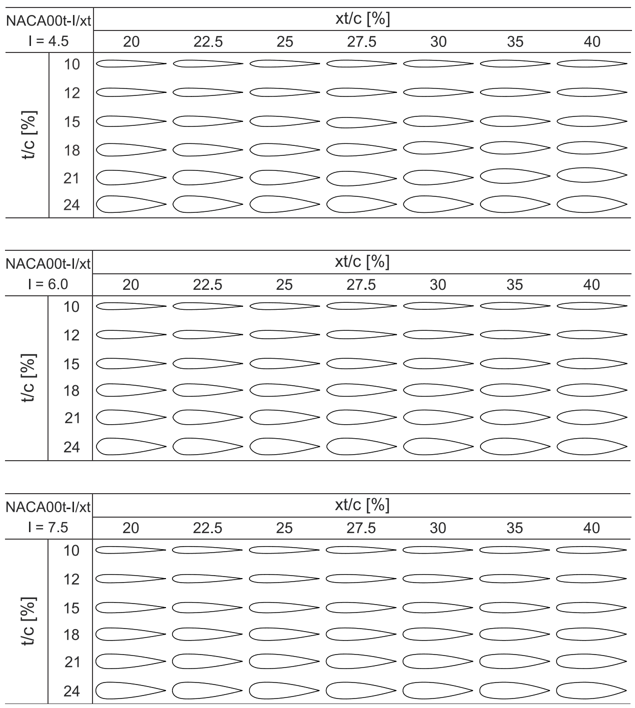

Figure 4: Studied airfoil shapes.

Note that any value of *I* out of the selected range results in a too sharp or too blunt leading edge. The analysis is based on 126 airfoil shapes (see Fig. 4). The modification of the airfoil coordinates and the related equations are documented in Ref. [39]. The focus of this study is on symmetric airfoils with zero camber. The morphing airfoils are designated as the *NACA00t/c – I / xt/c*. The first symbol from left to right, i.e., *t/c*, represents the maximum thickness in %c; the second one, *I*, shows the index of leading-edge radius (with one decimal precision); and the third one, *xt/c,* is the chordwise position of the maximum thickness in 10th of the

https://doi.org/10.5194/wes-2022-81
Preprint. Discussion started: 14 October 2022

chord with two decimal precision. For example, the NACA0024-4.5/3.50 has a maximum thickness of t/c = 24%, located at xt/c = 35%, and a leading-edge radius index of I = 4.5.

4. Results

The results are presented in two scenarios, namely, morphing airfoils as functions of λ (Sect. 4.1), and dθ (Sect. 4.2). In Sect. 4.3 the performance of the morphing airfoils from the first scenario is compared with that of the reference airfoil. A coupled analysis is performed at different λ of 2.5, 3.0, 3.5, 4.5 and 5.5. Figure 5 depicts the variation of α as the turbine passes through its last revolution. Note that the higher the value of λ is, the more limited the variation of α is. For λ = 2.5, 3.0 and 3.5 the variation of α exceeds the α_{ss} for all the studied airfoils, while at higher λ = 4.5 and 5.5, not for all the studied airfoils the same event is observed. The reader is referred to [57], where the method of calculating the α from the CFD results is provided in detail.

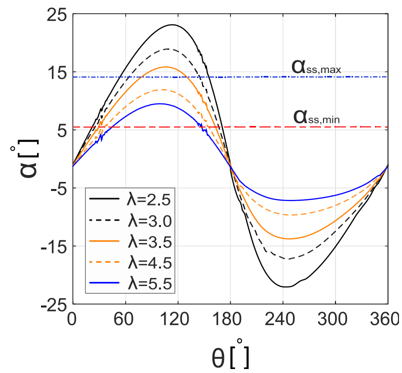

Figure 5: α versus θ for different λ. The $\alpha_{ss,min}$ and $\alpha_{ss,max}$ are based on Xfoil.

4.1 Morphing the airfoil shape-defining parameters

To derive the optimal airfoil for each λ, the combination of the t/c_{opt}, xt/c_{opt}, and I_{opt}, corresponding to the turbine $C_{P,max}$ is determined. Sect. 4.1.1 to 4.1.3 are devoted to the discussions on individual morphing, and Sect. 4.1.4, presents an overall view on the combined morphing of the aforementioned parameters.

4.1.1 Morphing the maximum thickness (*t/c*)

Figure 6 shows the impact of morphing t/c on the turbine C_P for the studied range of xt/c, I and λ. Figure 7 shows the instantaneous moment coefficient C_m versus θ for selected t/c and xt/c. It can be observed that:

Regarding the lowest value of I = 4.5 (see Fig. 6a – e and Fig. 7): Generally speaking, the trend of $C_P - t/c$ for different λ is similar, except for some noticeable differences. That is, by increasing λ, the C_P shows higher sensitivity to t/c. This is reflected as higher $|\Delta C_P|$ and can be due to the following reasoning: by morphing t/c, the pressure gradient changes over the airfoil; therefore, the transition point, the separation and stall characteristics, and eventually the resultant aerodynamic loads also change. However, when the flow is fully separated in the post-stall regime, morphing t/c has no longer significant impact on C_P. By increasing λ, and thus, more limited variation of α, the blade passes over a range of fewer azimuth angles in the post-stall regime (see Fig. 5). Due to this, morphing the t/c is influential within a wider range of effective θ. This can be recognized by the improved C_P for higher λ. At λ = 2.5, the C_P follows a polynomial trend for $xt/c \leq 30\%$, and a monotonic upward trend for $xt/c \geq 35\%$. Nevertheless, with the exception of $xt/c \leq 22.5\%$ at λ = 5.5, where the C_P monotonically decreases by increasing t/c, the trend remains polynomial for different values of xt/c at the studied range of λ. That is, by positive morphing of t/c, the C_P experiences an initial growth to its

https://doi.org/10.5194/wes-2022-81
Preprint. Discussion started: 14 October 2022

maximum value at t_{opt}/c, followed by a reduction for $t/c > t_{opt}/c$. This can be recognized from the C_m plots, where by morphing t/c to its optimal value at t_{opt}/c, the sudden drop in $C_{m,max}$, which indicates the instant of moment stall, is observed at higher θ; the consequent fluctuation is alleviated, and the overall value of C_m increases, thus, making consistency with the highest C_P at t_{opt}/c for a fixed xt/c (see Fig. 7a-i for selected xt/c). This can be attributed to the following observations from the skin friction, lift, and drag coefficients (C_f, C_l, and C_d): when the turbine is operating at low values of $\lambda \leq 3.5$, increasing t/c from 10% to t_{opt}/c, changes the stall type from leading-edge stall and thin-airfoil stall for $t/c \leq 12\%$ to trailing-edge stall for moderate- and high-thickness airfoils with $t/c \geq 15\%$; an earlier formation of laminar separation bubble (LSB) and trailing-edge separation (TES) is observed; TES-LSB merging (i. e., full-flow separation) is discovered to occur at higher azimuth, indicating a more extended favorable pressure gradient for t_{opt}/c; the dynamic stall characteristics (i. e., jump in lift and drag coefficients, and post-stall load fluctuation) are significantly reduced; and the deviation in lift and drag, which indicates the onset of dynamic stall, shifts to higher azimuth. However, an earlier stall is found to occur for $t/c > t_{opt}/c$ due to more pronounced earlier merging of TES-LSB. This is reflected by lower C_P and $C_{m,max}$ for $t/c > t_{opt}/c$ (see Figs. 6a-c and 7a-i). Note that the monotonic growth in $C_P - t/c$ for $xt/c \geq 35\%$ at $\lambda = 2.5$ can also be explained with the aforementioned reasoning, yielding the $C_{P,max}$ at the highest thickness of $t_{opt}/c = 24\%$ (see Fig. 6a). For brevity, the skin friction, lift, and drag coefficients are not presented here.

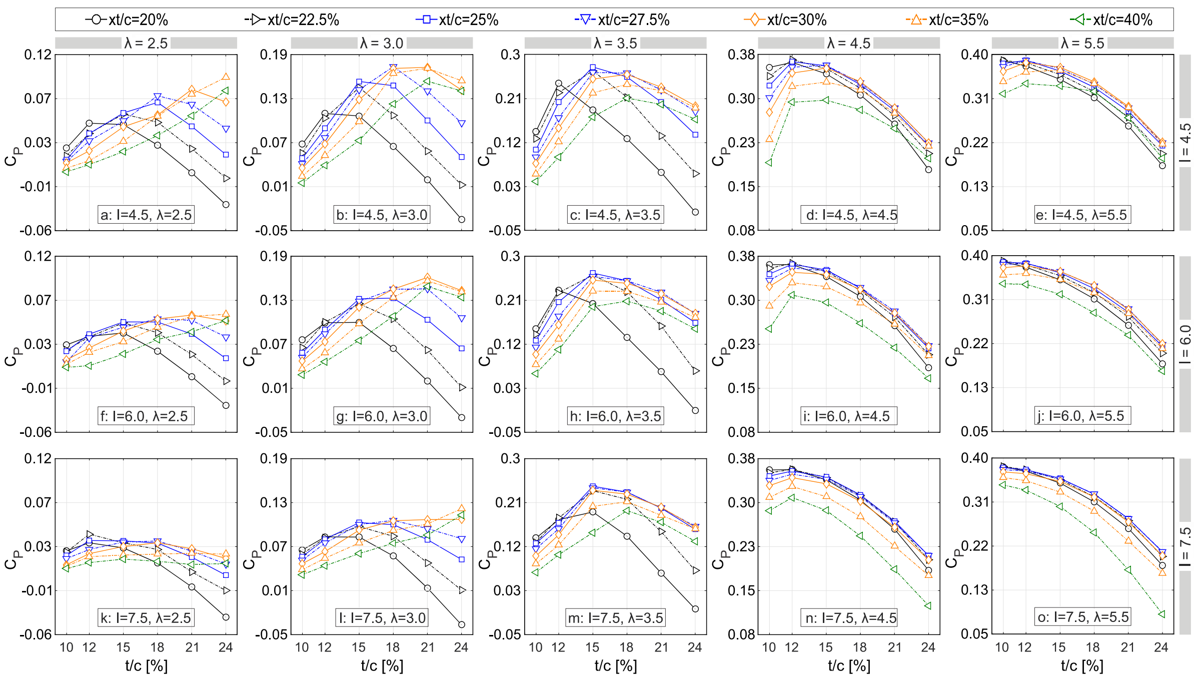

Figure 6: Impact of morphing t/c on the turbine C_P at different xt/c and λ.

Table 3 shows the t_{opt}/c, corresponding to each xt/c (i. e., $t_{opt,xt}/c$) at different λ. The t_{opt}/c corresponding to each λ is indicated by a star sign. It can be seen that by increasing xt/c, which means a longer favorable pressure gradient on the blade, a higher thickness is needed for the airfoil to be optimal. Note that, increasing λ, influences the shape of the optimal airfoil by decreasing its thickness. In other words, the higher λ is, the thinner the optimal airfoil is. This is consistent with the findings documented in [45, 64], where it shows the superior performance of thick airfoils at low λ. This may be attributed to the turbine operational regime as follows: When the turbine goes into regimes with higher λ and more pronounced reduction in the variation of α, higher values of C_l at lower α is of most impact on the turbine C_P. Therefore, thinner airfoils with a higher lift curve slope outperform the thicker ones with a

https://doi.org/10.5194/wes-2022-81
Preprint. Discussion started: 14 October 2022

lower slope of the $C_l - \alpha$. Eventually, this results in less pronounced sensitivity of the t_{opt}/c to xt/c, and shifting the peak in $C_P - t/c$ (i. e., t_{opt}/c) towards the lowest t/c = 10% and 12% in the non-dynamic stall regime with $\lambda \geq 4.5$ (see Table 3). The analysis also shows a drag increment for thicker airfoils at λ = 4.5 and 5.5, which is a result of the earlier formation of LSB and TES. This is consistent with the reduction in C_P and $C_{m,max}$ for $t/c > t_{opt}/c$ (see Figs. 6d-e and 7j-o). Note that for $xt/c \leq 22.5\%$ at λ = 5.5 the same reasoning results in a monotonic decrease of C_P, yielding the $C_{P,max}$ at the lowest thickness of t/c = 10%.

Regarding the moderate and highest values of I = 6.0 and 7.5 (see Fig. 6f-j and 6k-o): The overall trend for C_P is very similar to that of the lowest I = 4.5; however, it shows comparatively lower values of $|\Delta C_P|$), especially for $\lambda \leq 3.5$. The impact of morphing the r_{LE} on the turbine C_P is separately discussed in detail in Sect. 4.1.3; therefore, it is not included here.

Table 3. $t_{opt,xt}/c$ for different values of xt/c and λ (I = 4.5).

λ \ xt/c	20	22.5	25	27.5	30	35	40	*xt/c* [%]
2.5	12	15	18	18	21	24*	24	$t_{opt,xt}/c$ [%]
3.0	12	15	15	18*	21	21	21	
3.5	12	15	15*	15	18	18	18	
4.5	12	12*	12	15	15	15	15	
5.5	10	10*	12	12	12	15	12	

* t_{opt}/c at the corresponding λ

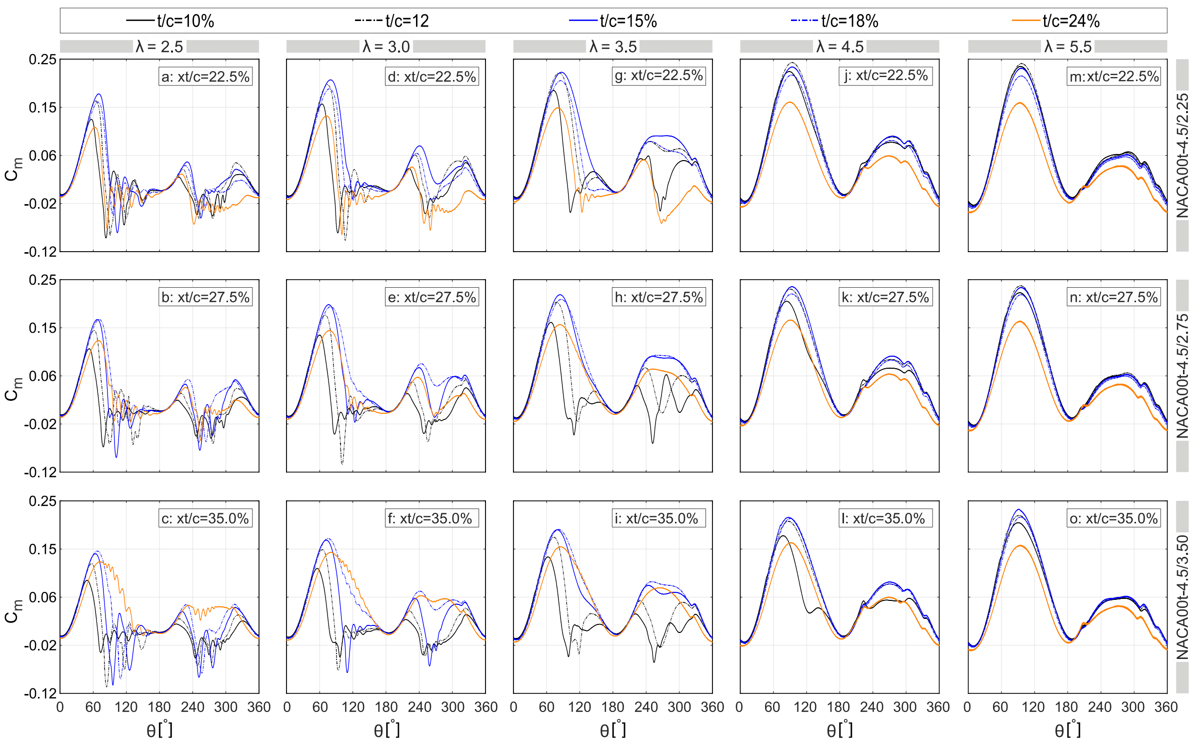

Figure 7: Impact of morphing t/c on the turbine C_m for selected xt/c and t/c at different λ.

4.1.2 Morphing the chordwise position of maximum thickness (xt/c)

Figure 8 shows the variation of the turbine C_P versus xt/c at the studied range of t/c, I, and λ. Figure 9 shows the instantaneous moment coefficient C_m versus azimuth for selected xt/c and t/c. It can be seen that:

https://doi.org/10.5194/wes-2022-81
Preprint. Discussion started: 14 October 2022

Regarding the lowest value of $I = 4.5$ (ee Fig. 8a-e): The overall trend of $C_P - xt/c$ for different λ is very similar, except for the following differences. By increasing λ, the turbine C_P shows higher $|\Delta C_P|$. This is due to the similar reasoning discussed earlier in Sect. 4.1.1, and summarized as follows: morphing the xt/c results in changing the boundary layer and stall characteristics. On the other hand, increasing λ is associated with lower variation of α, i.e., a more limited azimuthal range of the post-stall regime. As a result, the impact of morphing xt/c becomes significant over a wider range of θ, resulting in improved C_P.
For $t/c \leq 12\%$ in the dynamic stall regime with $\lambda \leq 3.5$, the C_P monotonically decreases by morphing the xt/c, yielding the $C_{P,max}$ with the lowest xt/c of 20% (see Fig. 8a-c). However, apart from $t/c = 10\%$ at $\lambda = 4.5$, where C_P monotonically decreases, the trend for thin airfoils changes to polynomial at $\lambda \geq 4.5$ (see Fig. 8d-e). In other words, by morphing xt/c from 20% to 40%, the C_P grows to its maximum value at xt_{opt}/c, before decreasing for $xt/c > xt_{opt}/c$. On one hand, the monotonic behavior of C_P for thin airfoils at low λ can be explained based on the observations of the skin-friction coefficient C_f as follows: The dynamic stall for $t/c \leq 12\%$ is preceded by either (i) gradual extension of the LSB towards the trailing edge (thin-airfoil stall), or (ii) a sudden upstream propagation of the TES (leading-edge stall). Morphing the xt/c to higher values results in either an earlier downstream extension of the LSB, or an earlier formation and abrupt-upstream propagation of the TES; and consequently, an advanced stall on the blade. This is evident from the C_m plots for $t/c = 12\%$ (see Fig. 9a-c), where the abrupt drop in $C_{m,max}$ occurs at a lower θ, indicating an earlier moment stall due to increasing the xt/c. The overall lower values of C_m for higher xt/c justify the monotonic reduction in C_P. This can also be recognized from the C_l and C_d plots, where by increasing xt/c, the deviation in lift and drag coefficients occurs at lower azimuth, signaling an earlier dynamic-stall onset. For brevity, the C_f, C_l, and C_d plots are not presented here.

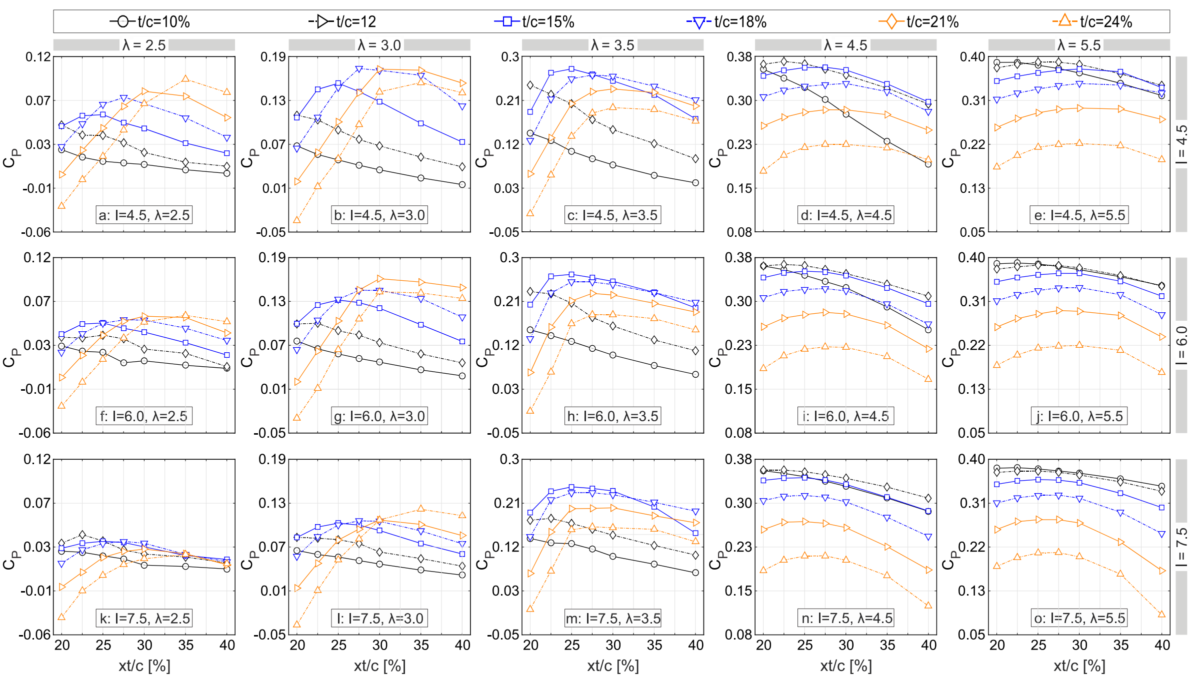

Figure 8: Impact of morphing xt/c on the turbine C_P at different t/c and λ.

On the other hand, the polynomial trend of C_P for thin airfoils at $\lambda \geq 4.5$ (i. e., non-dynamic stall regime) can be recognized from the C_m plots. For example, by morphing xt/c from 20% to $xt_{opt}/c = 25\%$ for $t/c = 12\%$ $\lambda = 5.5$, the $C_{m,max}$ slightly increases before decreasing for $xt/c \geq 27.5\%$ (see Fig. 8e). This can be explained by the skin-friction coefficient C_f, where it shows an earlier formation and upstream propagation of the TES, and thus, an earlier stall for $xt/c > xt_{opt}/c$. Note that, when the adverse effects of

https://doi.org/10.5194/wes-2022-81
Preprint. Discussion started: 14 October 2022

dynamic stall are suppressed at $\lambda \geq 4.5$, increasing *xt/c* shows a marginal positive impact on the C_P for thin airfoils, reflecting a polynomial trend of C_P versus *xt/c*. However, the value of *t/c* for thin airfoils plays a more crucial role in this regime. This can be observed from the sharp downward trend of C_P – *xt/c* for *t/c* = 10% at λ = 4.5, while it changes to a polynomial trend for *t/c* = 12%. This may be attributed to the more pronounced formation and propagation of TES, and thus, an earlier stall due to increasing *xt/c* for *t/c* = 10%. However, the trend of C_P – *xt/c* for *t/c* of 10% remains polynomial at λ = 5.5, showing less sensitivity to TES at higher λ. For brevity, C_f contour plots are not presented here.

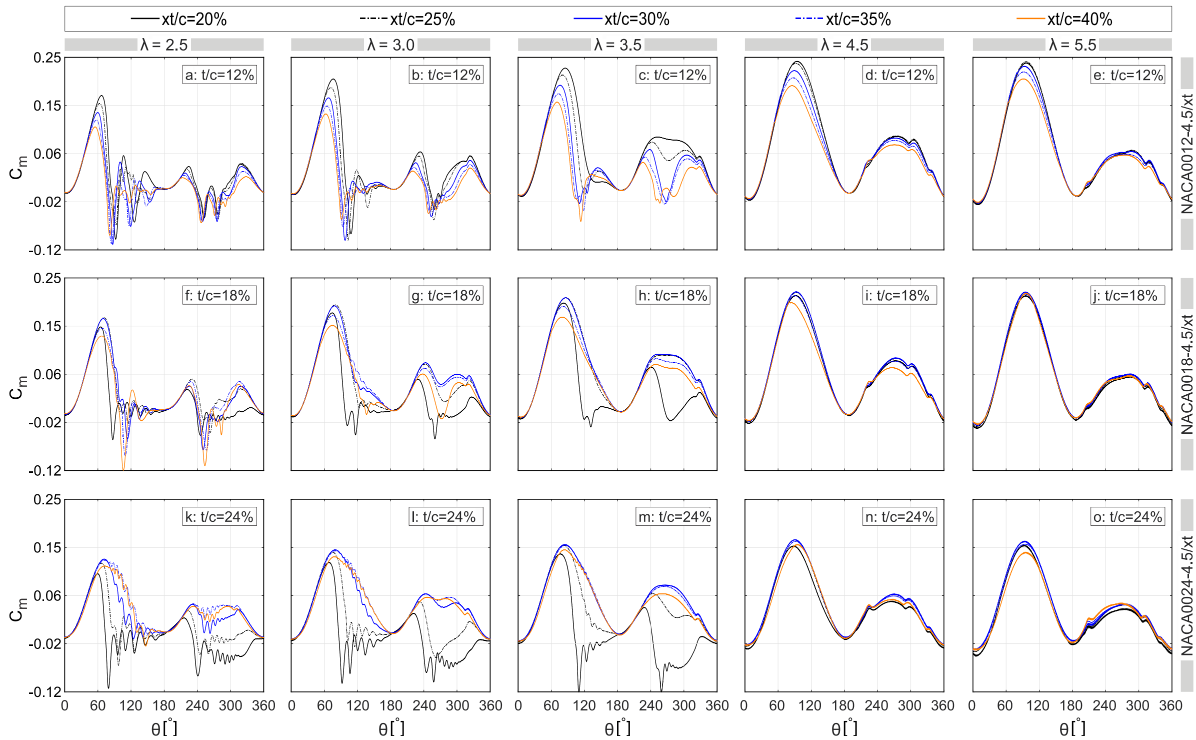

Figure 9: Impact of morphing *xt/c* on the turbine C_m for selected *t/c* and *xt/c* at different λ.

For the medium- and high-thickness airfoils (i.e., *t/c* ≥ 15%), the turbine C_P polynomially increases with *xt/c* (see Figs. 8a-e). As previously discussed in Sect. 4.1.1, this polynomial trend is a consequence of thicker-airfoil stall type, which is triggered by the formation of a flow reversal near the trailing edge [65-68]. Therefore, when *xt/c* morphs to its optimal value, the adverse pressure gradient becomes less severe, resulting in improved stall characteristics. This can be recognized by either dynamic stall alleviation at low values of $\lambda \leq 3.5$, or a postponed stall at non-dynamic stall regimes with $\lambda \geq 4.5$. Table 4 gives the $xt_{opt,t}/c$ (i. e., the xt_{opt}/c at each *t/c*) in terms of $C_{P,max}$ for each λ. The corresponding xt_{opt}/c for different λ is indicated by a star sign. For $\lambda \leq 3.5$, by increasing *t/c*, the $xt_{opt,t}/c$ also increases. However, by increasing λ from 2.5 to 3.5, and thus, encountering a comparatively lighter dynamic stall and more limited variation of α, the xt_{opt}/c and its corresponding *t/c* decrease (see also Fig. 8). The reason for the outperformance of thin airfoils at higher λ is explained earlier in Sect. 4.1.1. Nevertheless, in the dynamic stall regime, the outperformance of moderate to high values of *xt/c* for thicker airfoils at a fixed λ is readily apparent from the turbine C_m for selected *t/c* = 18% and 24% (see Fig. 9f-h and k-m). It can be seen that increasing *xt/c* to its optimal value results in an increase in the C_m curve peak, a delay in the sudden drop of $C_{m,max}$, less pronounced subsequent fluctuations, and higher values of C_m in the turbine downwind quartile. This is due to either alleviated dynamic stall, and is more pronounced for *t/c* = 24% (see Fig. 9k-m). A further

https://doi.org/10.5194/wes-2022-81
Preprint. Discussion started: 14 October 2022

increase in $xt/c > xt_{opt}/c$, is found to have a negative effect on C_m and finally leads to an earlier stall. This can be explained by the C_f contour plots, where increasing xt/c higher than xt_{opt}/c promotes the formation of LSB and TES, and results in an earlier full-flow separation and drop in $C_{l,max}$. Please note that for better illustration, the C_m plots are not presented for all the studied values of xt/c. For $\lambda \geq 4.5$, by morphing xt/c for $t/c \geq 15\%$, the C_P shows less sensitivity to xt/c and the corresponding xt_{opt}/c changes marginally (see Fig. 8d-e and Table 4). This is consistent with the turbine C_m plots for selected t/c = 18% and 24%, where the $C_{m,max}$ and the azimuth of moment stall are almost invariant to xt/c (see Fig. 9i-j and Fig. 9n-o).

Regarding the moderate and highest values of I = 6.0 and 7.5 (see Fig. 8f-j and 8k-o): The $C_P - xt/c$ shows a similar trend to that of I = 4.5. However, in dynamic stall regime (i.e., $\lambda \leq 3.5$), the turbine C_P shows a considerably smaller $|\Delta C_P|$, especially for higher xt/c. On the other hand, in non-dynamic stall regime with $\lambda \geq 4.5$, a marginal reduction in $|\Delta C_P|$ is observed. However, the $C_P - xt/c$ shows more pronounced sensitivity to morphing xt/c for the moderate and thick airfoils.

Table 4. $xt_{opt,I}/c$ for I = 4.5 at different t/c and λ.

λ \ t/c [%]	10	12	15	18	21	24	
2.5	20	20	25	27.5	30	35*	$xt_{opt,I}/c$ [%]
3.0	20	20	25	27.5*	30	35	
3.5	20	20	25*	27.5	30	30	
4.5	20	22.5*	27.5	30	27.5	27.5	
5.5	22.5*	25	30	30	30	30	

* xt_{opt}/c at the corresponding λ

4.1.3 Morphing the leading-edge radius (r_{LE})

Figure 10 shows the impact of morphing r_{LE} on the C_P for selected and optimal airfoils at different λ. Figure 11 shows a comparison of the $C_P - xt/c$ for different I and selected values of t/c. The analysis is grouped based on the maximum thickness as follows:

Regarding the thin airfoils (t/c = 10% and 12%) (see Fig. 10 and 11a-e): regardless of xt/c, the turbine C_P is marginally influenced by the r_{LE}. This can be attributed to the low dependency of thin airfoils and the relevant aerodynamic loads on r_{LE}, which is due to the geometrical constraints imposed by the airfoil thickness. It can be observed that by increasing the index of r_{LE} for different xt/c at $\lambda \leq 3.5$, C_P slightly changes; this minimal difference is in line with the corresponding C_m plots for $t/c \leq 12\%$. This can also be recognized from the skin friction, lift, and drag coefficients by the negligible changes in the characteristics of boundary layer events, including LSB and TES, and consequently the onset of dynamic stall and $C_{d,max}$. Due to the large volume of the results, the C_m, C_l, C_d, and C_f plots are not presented here. For $\lambda \geq 4.5$, except for the NACA0010-I/3.5, where increasing r_{LE} has the most influence on C_P, the aerodynamic loads and the turbine C_m show even less sensitivity to r_{LE}. Note that this is the regime in which the dynamic stall is no longer encountered and thin airfoils outperform the rest of the airfoils. The impact of r_{LE} on the turbine C_P for the optimal thin airfoils at $\lambda \geq 4.5$ is shown in Fig. 10f. Figures 12d and e show the corresponding C_m plots.

Regarding the moderately-thick airfoils (t/c = 15% and 18%) (see Fig. 10 and 11f-j): overall, the turbine C_P shows higher dependency and sensitivity to r_{LE}. The higher dependency is due to the less severe geometrical constraints imposed by the moderately thick airfoils. Thus, morphing the r_{LE} noticeably modifies the airfoil shape and thereby influences the aerodynamic loads. The higher sensitivity is reflected by the noticeable monotonic reduction of C_P for most of the xt/c values. This significant decrease can be recognized from the C_m plots, where the curve peak drops by morphing the leading edge to more blunt shapes (i. e., higher r_{LE}). This may be due to the promoted LSB and TES characteristics, which result in higher $C_{d,max}$ for larger r_{LE}. For $\lambda \leq$ 3.0, the more prominent sensitivity is observed within the range of $22.5\% \leq xt/c \leq 35\%$; however, the C_P shows less sensitivity to r_{LE} for λ = 3.5, corresponding to a lighter dynamic stall regime (see Fig. 11f-h). Note that the moderately thick airfoils show superior performance over the thin and thick airfoils at λ = 3.0 and 3.5 (i. e., the NACA0018-4.5/2.75 and NACA0015-4.5/2.5, respectively). Figure 10f and Figs. 12b and c show the impact of morphing r_{LE} on the turbine C_P and C_m for the optimal airfoils at

https://doi.org/10.5194/wes-2022-81
Preprint. Discussion started: 14 October 2022

λ = 3.0 and 3.5. When the turbine goes into the non-dynamic stall regime with $\lambda \geq 4.5$, the range of *xt/c* within which the index of leading-edge radius is the most influential, shifts downstream to 30% ≤ *xt/c* ≤ 40% (see Fig. 11i and j).

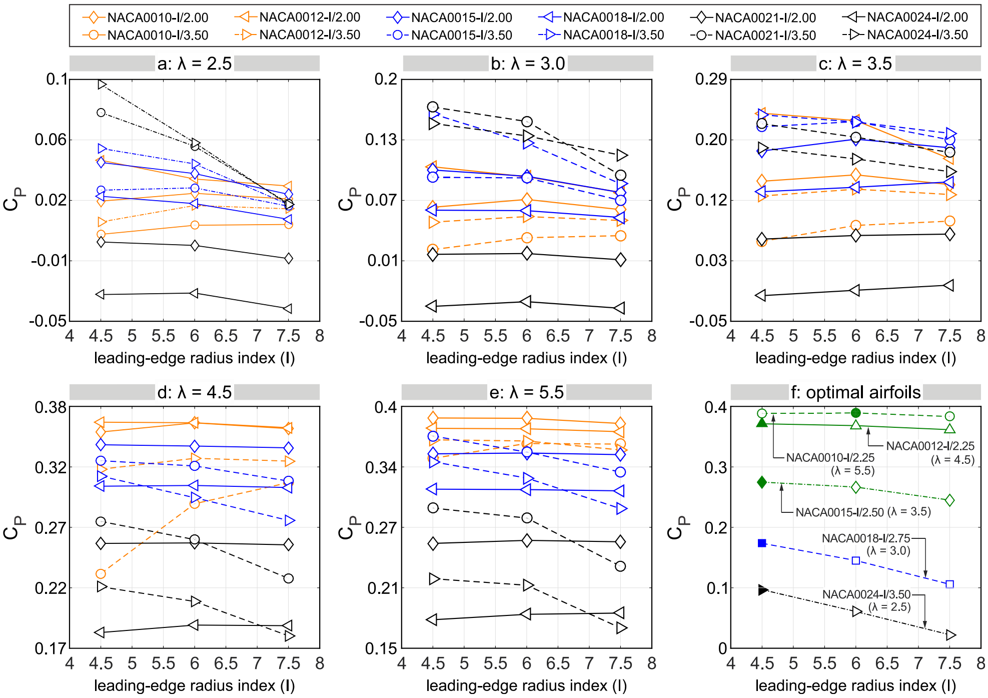

Figure 10: Impact of morphing r_{LE} on the C_P for (a-e) selected, and (f) optimal airfoils at different λ. Filled symbols represent the optimal airfoils corresponding to each λ.

Regarding the thick airfoils (t/c = 21% and 24%) (see Fig. 10 and 11k-o): the analysis shows that at λ = 2.5, thick airfoils significantly surpass other airfoils in terms of power performance (see Fig. 10). Aside from the following differences, the overall trend of $C_P - xt/c$ is quite similar to that of moderately thick airfoils: C_P values are more sensitive to r_{LE} at λ = 2.5, 4.5 and 5.5, but less so at λ = 3.0 and 3.5 (see Fig. 11k-o). By increasing the r_{LE}, the C_P values experience a monotonic reduction, especially for thick airfoils with *xt/c* ≥ 30% at λ = 2.5, where the variation of *I* is the most influential on C_P. For example, the overall reduction of C_P for the NACA0024-*I*/3.50 at λ = 2.5, 3.0, 3.5, 4.5 and 5.5 is 77%, 21%, 17%, 19% and 23%, respectively. This can be recognized from the C_m plots, where the C_m values decrease dramatically in both upwind and downwind quartiles, the C_m curve peak drops, and the post-stall C_m fluctuation gets more significant (see Fig. 12a). This is due to earlier formations of the LSB and TES, and thus a higher $C_{d,max}$. Thick airfoils with low *xt/c* show marginal sensitivity to r_{LE} at different λ. The corresponding C_m plots show approximately the same azimuth of moment stall for different *I*. For brevity, the C_m plots are only presented for the NACA0024-*I*/3.50, which is the optimal airfoil at λ = 2.5 (see Fig. 12a).

Overall, at $\lambda \leq 3.5$, the xt_{opt}/c belongs to the range of *xt/c*, which corresponds to the highest sensitivity of C_P to r_{LE}. For example, the optimal airfoil at λ = 2.5 (i. e., the NACA0024-4.5/3.5) has *xt/c* = 35% that fits in the range of 30% ≤ *xt/c* ≤ 40%, within which the impact of r_{LE} is the most significant. This is while the xt_{opt}/c for $\lambda \geq 4.5$ (i. e., *xt/c* = 22.5%) does not belong to such a range of *xt/c* (i. e., *xt/c* ≥ 30%). In addition, the most noticeable improvement in C_P due to morphing the r_{LE} occurs at λ = 2.5, where the dynamic stall deeply affects the aerodynamic and power performance of the blade. Nevertheless, by increasing λ and thus, alleviating or avoiding the dynamic stall, the aerodynamic loads are less affected by the r_{LE}.

https://doi.org/10.5194/wes-2022-81
Preprint. Discussion started: 14 October 2022

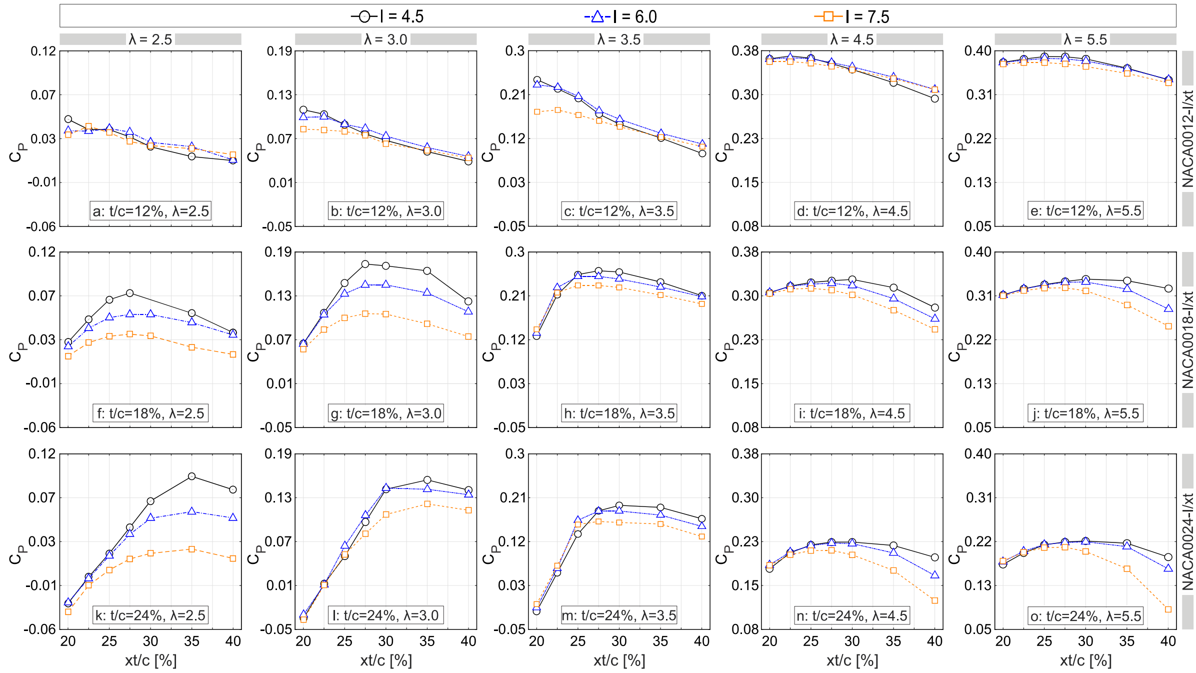

Figure 11: Comparison of the turbine C_P versus xt/c for different I and λ.

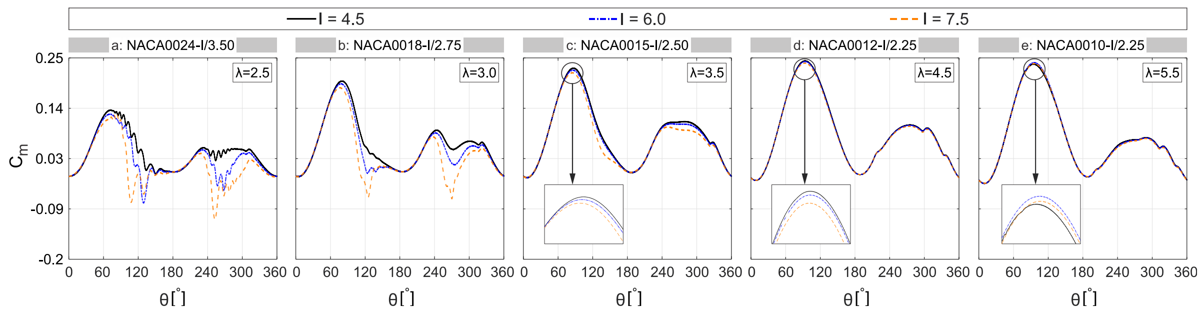

Figure 12: Impact of morphing r_{LE} on the turbine C_m for the combination of t_{opt}/c and xt_{opt}/c at different λ.

4.1.4 Combined morphing of the airfoil shape-defining parameters

Morphing the airfoil shape-defining parameters is thought to have a fully coupled impact on the turbine C_P. Thus, it is of high importance to study the impact of their combined morphing on the turbine C_P and C_T. Figure 13 shows the variation of C_P in $t/c - xt/c$ space for different I and λ. Except for $\lambda = 5.5$, where the combination of t_{opt}/c and xt_{opt}/c is achieved by the moderate $I = 6.0$, the $C_{p,max}$ corresponds to the smallest $I = 4.5$ for $\lambda \leq 4.5$.

For $\lambda = 2.5$ and $I = 4.5$, the global optimum occurs by a set of high t/c and xt/c (i.e., NACA0024-4.5/3.50). For higher $I = 6.0$, although the combination of t_{opt}/c and xt_{opt}/c remains invariant, the local optimum area is found to morph into thin airfoils with low xt/c. For $I = 7.5$, the morphing airfoil changes to a thin airfoil with low xt/c, while experiencing lower C_P. The variation of optimal airfoil shape-defining parameters for different λ and the resultant airfoils at each λ are illustrated in Fig. 14.

At $\lambda = 3.0$, the local region of $C_{P,max}$ shows less sensitivity to I, shifting between moderate and high values of t/c and xt/c (see Fig. 13d-f). However, similar to that of $\lambda = 2.5$, the overall range of C_p values narrows down with increasing I. For $\lambda = 3.5$, the local optimum region remains nearly the same at moderate values of t/c and xt/c for different I (see Fig. 13g-i); while for higher values

https://doi.org/10.5194/wes-2022-81
Preprint. Discussion started: 14 October 2022

of $\lambda \geq 4.5$, it stays approximately independent of *I*, shifting marginally between low values of *t/c* and *xt/c* (see Fig. 13j-o). This implies that, by increasing λ, the local optimum region is less sensitive to *I*. In other words, the higher λ is, the less dependent the local optimum is on *I*. Overall, by increasing λ the local region of optimal airfoil shapes changes from the combination of high values of *t/c* and *xt/c* for $\lambda = 2.5$ to moderate *t/c* and *xt/c* for $\lambda = 3.0$ and 3.5, and low values of *t/c* and *xt/c* for $\lambda \geq 4.5$.

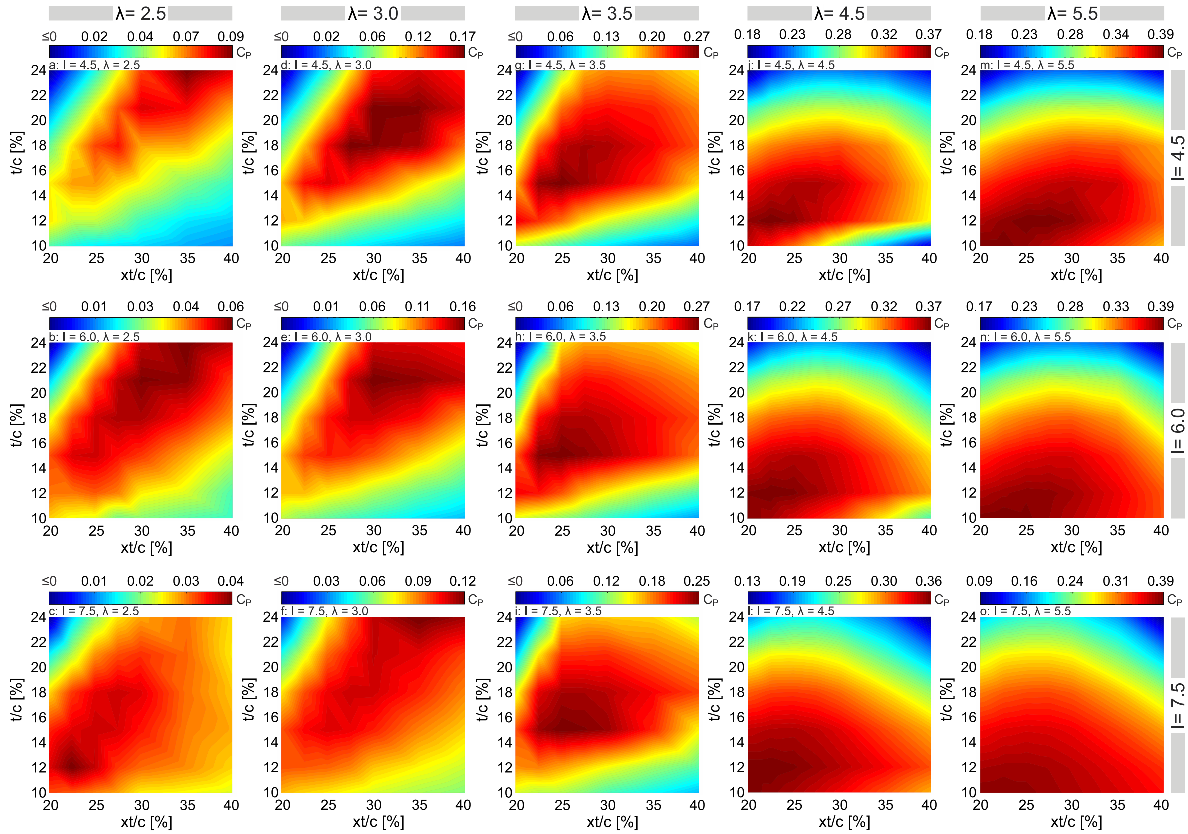

Figure 13: Turbine C_P in *t/c* – *xt/c* space. Each contour plot is based on 42 simulations. Colormaps are in different range.

It is observed that in designing morphing blades, single-parameter studies will not provide the overall picture and could lead to unreliable results. The contour plots give a conceptual view of the optimal regions in terms of the airfoil shape-defining parameters, with which the resultant airfoils have their most efficient performance; and also, the inefficient regions of the turbine C_P, which must be avoided.

Figure 15 shows the turbine C_T in *t/c* – *xt/c* space. It is interesting to observe that for low $\lambda \leq 3.5$ there is no coincidence between the optimal regions of C_T and C_P contours; while for $\lambda \geq 4.5$, these two regions overlap. By increasing λ, the optimal region extends marginally towards higher *t/c* and *xt/c*, while also experiencing higher values of C_T. The noncongruent region of $C_{p,max}$ and $C_{T,max}$ at low values of λ is different from what is observed in the case of HAWTs. That is, the maximum power output of a HAWT occurs where the highest thrust load is exerted by the turbine blade on the flow. This led to a correlation between the optimal regions of C_P and C_T. In contrast, the results of the present study show that for VAWTs, the same phenomenon only occurs at high values of $\lambda \geq 4.5$, where the turbine goes into non-dynamic stall regimes with more limited variations of α. Therefore, when designing morphing blades for VAWTs, the C_T values corresponding to high values of λ are of more importance compared to those of lower λ, where dynamic stall is expected to occur.

https://doi.org/10.5194/wes-2022-81
Preprint. Discussion started: 14 October 2022

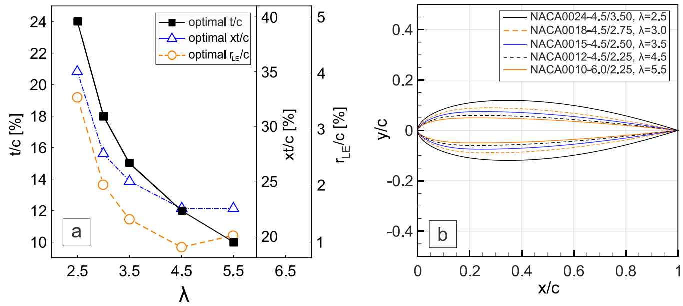

Figure 14. (a): variation of morphing airfoil shape-defining parameters and (b): morphing airfoils at different λ.

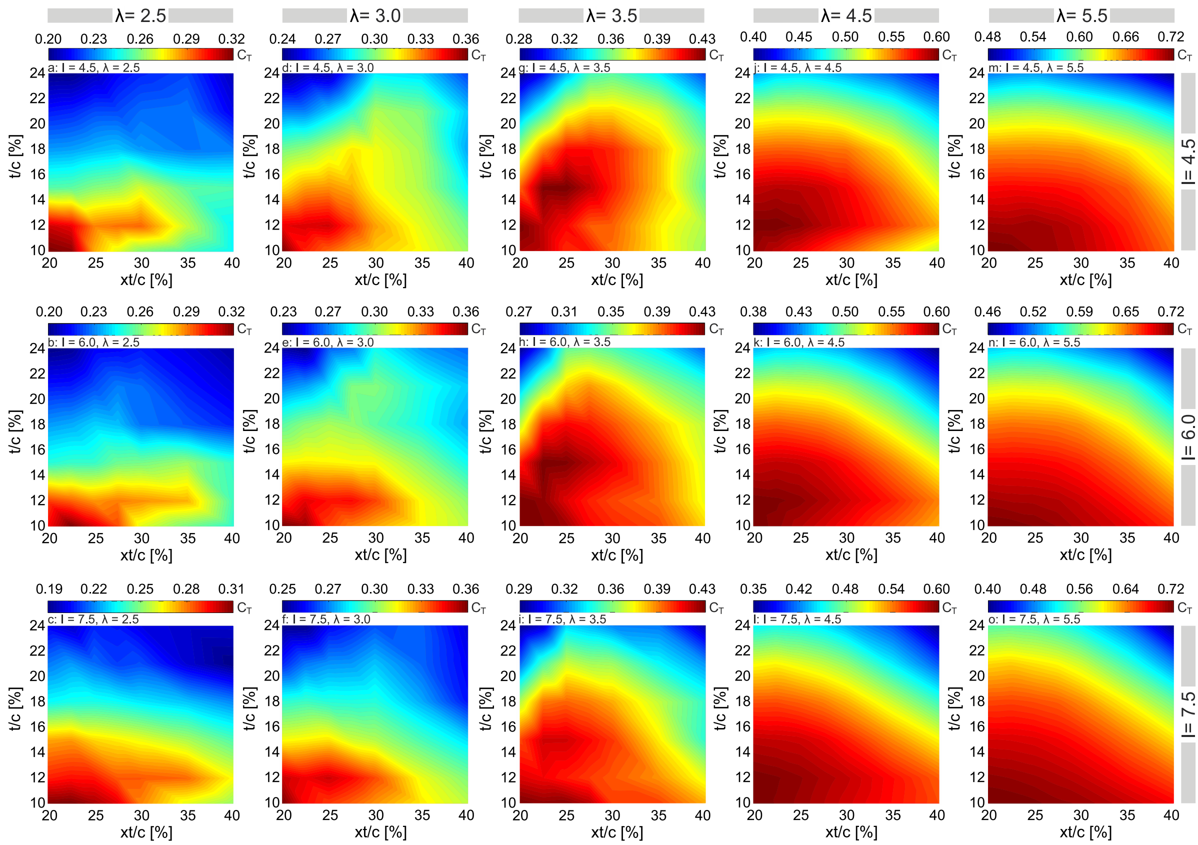

Figure 15: Turbine C_T in t/c – xt/c space. Each contour plot is based on 42 simulations. Colormaps are in different range.

4.2 Towards a morphing blade

This section provides an overview of the turbine power gain due to different morphing scenarios, namely a fixed optimal airfoil for each λ (scenario 1), as already discussed in Sect. 1; and an optimal airfoil for each $d\theta$, as discussed in the following Sect. (scenario 2). Figure 16 shows the variation of t/c and xt/c versus azimuth for scenario 2. Figure 17 shows the corresponding $C_{m,max}$ for each scenario in λ – θ space. Note that scenario 2 is divided into three cases, namely cases A, B and C. In cases A and B, the t_{opt}/c and xt_{opt}/c of the already identified optimal shapes for each λ are kept fixed and distributions of xt/c and t/c versus θ, corresponding to $C_{m,max}$, are extracted, respectively. In case C, the combination of t_{opt}/c and xt_{opt}/c, corresponding to $C_{m,max}$ at each $d\theta$ is selected and kept fixed, and distributions of xt_{opt}/c (i.e., case C1) and t_{opt}/c (i.e., case C2) versus azimuth are extracted,

https://doi.org/10.5194/wes-2022-81
Preprint. Discussion started: 14 October 2022

respectively. Note that I_{opt} = 4.5 remains invariant for $\lambda \leq 4.5$ and changes to I_{opt} = 6.0 only at λ = 5.5. For the sake of clarity and analysis, I_{opt} = 4.5 is assumed to be constant throughout the studied range of λ, introducing the NACA0012-4.5/2.50 as the optimal airfoil at λ = 5.5. The absolute difference between the $C_{P,max}$ values for optimal airfoils with I = 4.5 and 6.0 at λ = 5.5 is 0.0005.

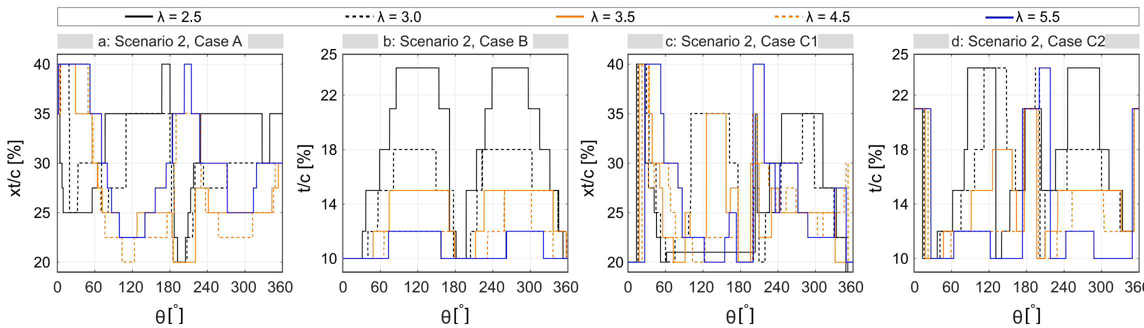

Figure 16: Morphing (a) *xt/c* and (b) *t/c* versuss azimuth for fixed t_{opt}/c and xt_{opt}/c corresponding to each λ; morphing (c) xt_{opt}/c and (d) t_{opt}/c vs azimuth for fixed t_{opt}/c and xt_{opt}/c corresponding to each $d\theta$.

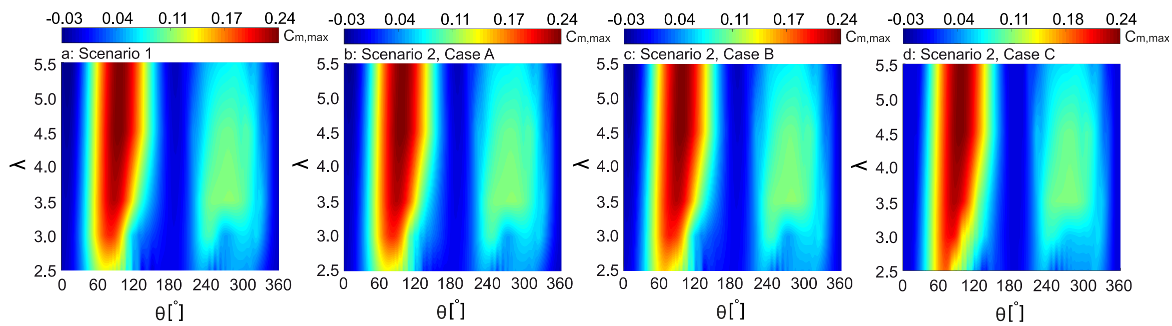

Figure 17: Turbine C_m in $\lambda - \theta$ space for different morphing scenarios.

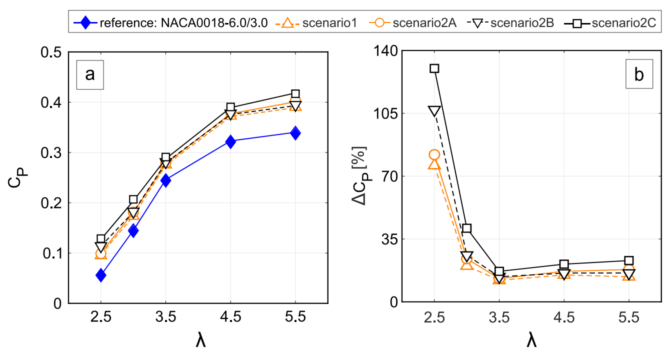

Figure 18: Variation of (a): Turbine C_P and (b): power gain due to different scenarios of a morphing blade at different λ.

Figures 16a and 17b show the results for scenario 2, case A. Note that the results correspond to the $C_{m,max}$ at each $d\theta = 0.1°$. It can be observed that *xt/c* shows almost the same level of sensitivity to θ for different λ (see Fig. 15 a). Fig. 17b shows the overall view of the $C_{m,max}$ as the blade section rotates and morphs at different λ. Obviously, the maximum torque is obtained around $\theta = 90°$ for different λ. The higher torque generated in the upwind quartile is due to the unperturbed upstream wind profile, while the less pronounced $C_{m,max}$ in the downwind quartile is due to the lower wind velocity and blade-wake interaction.

For scenario 2, case B, the observed trend for $t_{opt}/c - \theta$ is quite similar at different λ, except for a noticeable difference; that is, the higher λ is, the less sensitive the variation of t_{opt}/c to θ is. By increasing λ, and thus, decreasing the xt_{opt}/c, thinner airfoils outperform the thicker ones. The turbine $C_{m,max}$ shows negligible changes (see Figs. 16b and 17b). The observations for scenario 2C1 and C2

https://doi.org/10.5194/wes-2022-81
Preprint. Discussion started: 14 October 2022

Open Access
WIND ENERGY SCIENCE DISCUSSIONS

are almost similar to those of cases A and B, respectively. However, there are some narrow ranges of θ at the beginning, middle, and end of the turbine rotation disk, where noticeable differences exist. The resulting $C_{m,max}$ in $\lambda - \theta$ space differs slightly from the other scenarios (see Fig. 17d).

Figure 18 shows the turbine C_P and the power gain due to different scenarios for a morphing blade versus the reference case at different λ. By increasing λ from 2.5 to 3.5, the power gain significantly decreases. Nevertheless, for $\lambda \geq 4.5$ it marginally increases. The more pronounced ΔC_P at low λ is due to alleviating the dynamic stall by using a morphing blade. The averaged improvement in C_P due to scenarios 1, 2A, 2B, and 2C ($\overline{\Delta C_P}$) over the studied range of λ is 0.04, 0.045, 0.047, and 0.06, respectively.

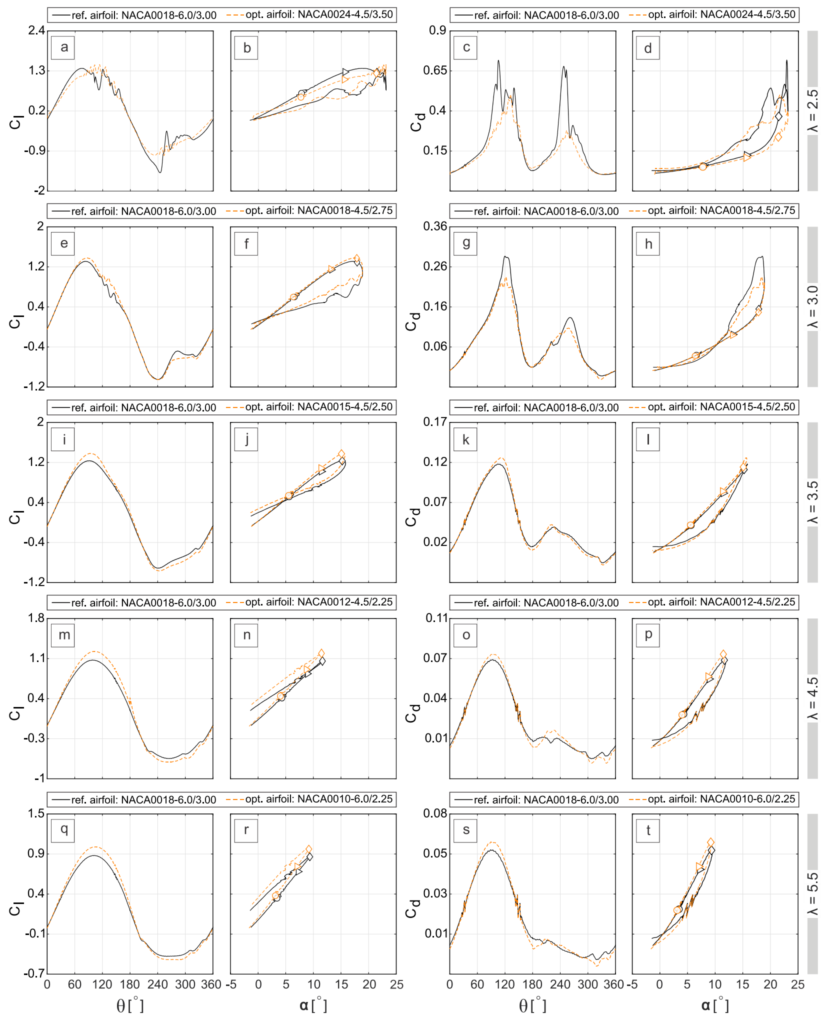

Figure 19: C_l and C_d versus θ and α for the reference and morphing airfoils at different λ (○: $\theta = 60°$; ▷: $\theta = 120°$; ◇: $\theta = 180°$).

4.3 Aerodynamic analysis of the morphing airfoils

Figure 19 gives a comparison of the turbine aerodynamic loads (namely, C_l and C_d) versus θ and α for the reference and morphing airfoils. The results correspond to scenario 1, where an optimal airfoil is identified for each λ. In general, the morphing airfoils have higher $C_{l,max}$ compared to that of the reference case. For λ = 2.5, the morphing airfoil shows an obvious reduction in drag

https://doi.org/10.5194/wes-2022-81
Preprint. Discussion started: 14 October 2022

jump both in upwind and downwind quartiles and reduced post-stall fluctuation. These are the reflections of the significantly-alleviated dynamic stall. Table 5 gives the $C_{l,max}$ and $C_{d,max}$ values for the reference and morphing airfoils at different λ. It can be seen that for λ = 3.0 and 3.5, where the turbine goes into a lighter-dynamic stall regime, the morphing airfoil shows higher $C_{l,max}$ with less severe post-stall fluctuation and lower $C_{d,max}$ with less substantial drag jump. For $\lambda \geq 4.5$ (i. e., non-dynamic stall regime), although the morphing airfoils show higher values for both the $C_{l,max}$ and $C_{d,max}$, the increase in $C_{l,max}$ is more dominant than that of the $C_{d,max}$ (see also Table 5). Figure 20 shows the turbine C_m for the reference and morphing airfoils at each λ. Other than a reduction for $0° \leq \theta \leq 80°$ at λ = 2.5, the turbine C_m is found to improve moderately due to the morphing airfoils at the studied range of λ, indicating higher turbine C_P.

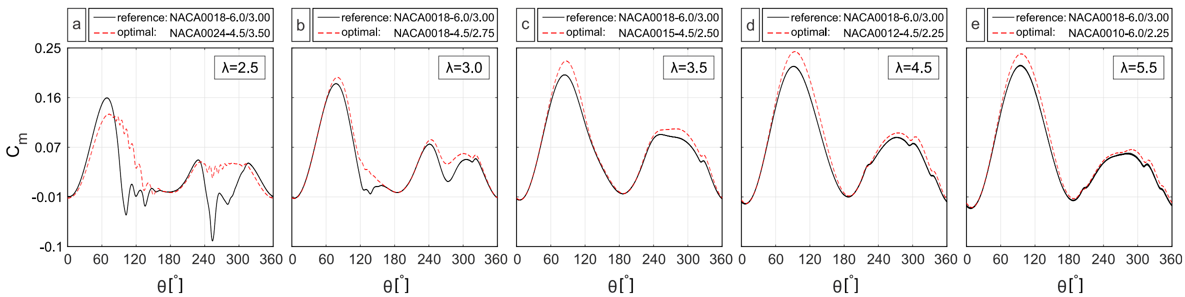

Figure 20: Turbine C_m for the reference and morphing blades at different λ (scenario 1).

Table 5. Estimated $C_{l,max}$ and $C_{d,,max}$ for the morphing and reference airfoils at different λ (scenario1).

λ	2.5		3.0		3.5		4.5		5.5	
load coefficient	$C_{l,max}$	$C_{d,max}$	$C_{l,max}$	$C_{d,max}$	$C_{l,max}$	$C_{d,max}$	$C_{l,max}$	$C_{d,max}$	$C_{l,max}$	$C_{d,max}$
reference	1.37	0.716	1.31	0.29	1.23	0.118	1.07	0.076	0.93	0.064
morphing	1.47	0.503	1.38	0.24	1.38	0.126	1.23	0.082	1.05	0.059
Difference [%]	+7	-29.8	+5	-17	+12	+6.7	+15	+8	+13	+8.5

5. Discussion

The present work includes a wide range of λ, where the turbine goes into different operational regimes of light-, deep-, and non-dynamic stall regimes. The aim of the analysis is to highlight the power gain of VAWTs due to different scenarios of a morphing blade. It is suggested to continue this work for the rest of important geometrical parameters, such as camber and its position along the chord, which describe the airfoil asymmetry and have the potential to morph.

The symmetric modified NACA 4-digit airfoil series is chosen as a basis for the morphing airfoils. The airfoils are generated by setting the three main defining parameters, i.e., t/c, xt/c and r_{LE}.

The results prove the usefulness of the morphing technique to improve the power performance of VAWTs as the main objective of this work. Also, the structural strength of the blade could be another important objective that must be considered while designing morphing blades for VAWTs. It is found that this objective is also satisfied, and the blade structural limitations are met. This is due to the fact that the morphing airfoil changes from a thin airfoil for the highest λ, corresponding to low wind speeds and aerodynamic loads, to a more robust thick airfoil for the lowest λ, where the lack of strength and stiffness can cause blade failure, and thus, the blade needs to withstand the aerodynamic loads and to avoid the resultant deflections. However, technical considerations related to the complexity of the electromechanical actuators for the morphing blade must be taken into account. The required actuators need to be chosen such that they can meet the displacement requirements at the corresponding response times and rotational speeds. In addition, it is of particular importance to consider the cost factor and feasibility of such a system and also to estimate the difference between the power required to drive the actuators and the resulting turbine power gain.

6. Conclusions

Incompressible URANS simulations, validated with experiments, are used to study the impact of different scenarios of a morphing blade on the power and thrust performance of a VAWT. Three main airfoil shape-defining parameter, namely *t/c*, *xt*/c and *I*, are chosen and morphed as functions of λ and θ to determine the optimal airfoils in terms of C_P in a wide range of λ.

The main conclusions are as follows:

- For each λ, there exists a morphing airfoil shape, corresponding to the turbine $C_{P,max}$. At the lowest λ = 2.5, the morphing airfoil is defined with *t/c* = 24%, *xt/c = 35%* and *I* = 4.5 (i.e., the NACA0024-4.5/3.5). In comparison to the baseline airfoil (i.e., the NACA0018-6.0/3.0), this airfoil has a smaller leading-edge radius; and a higher maximum thickness, which is found to shift downstream of the default point by 5%.
- By increasing λ, the combination of t_{opt}/c and xt_{opt}/c morphs to lower values; however, it shows less dependency on r_{LE}. For λ = 3.0, 3.5, 4.5, and 5.5, the optimal airfoil morphs to NACA0018-4.5/2.75, NACA0015-4.5/2.50, NACA0012-4.5/2.25 and NACA0010-6.0/2.25, respectively.
- Regarding the morphing airfoil as a function of θ, the highest average improvement in the turbine C_P is due to scenario 2C, where the combination of t_{opt}/c and xt_{opt}/c, corresponding to the turbine $C_{m,max}$ at each $d\theta$, is selected and kept fixed.
- The improvement in C_P due to morphing blade becomes more pronounced for low values of λ, where the adverse effects of dynamic stall, i.e., jump in aerodynamic loads and post-stall loads fluctuation, are mitigated by morphing airfoils.

The presented work not only highlights the strong relevance of the gain in turbine C_P to a morphing blade scenario but also emphasizes the combined morphing of the airfoil shape-defining parameters. That is, single-parameter morphing will not result in the highest power improvement of VAWTs. Other important considerations, such as morphing the rest of the geometrical parameters, are yet to be determined. Therefore, the present study could be a significant stride towards future studies on designing advanced morphing blades for smart VAWTs.

Acknowledgement

The first author acknowledges the support from his home university for the use of supercomputing facilities. The second author is currently a postdoctoral fellow of the Research Foundation – Flanders (FWO) and is grateful for the financial support (project FWO 12ZP520N).

References

1. Debiasi, M., et al., *Shape Change of the Upper Surface of an Airfoil by Macro Fiber Composite Actuators*, in *29th AIAA Applied Aerodynamics Conference*.
2. Wang, W., et al., *A Simplified Morphing Blade for Horizontal Axis Wind Turbines.* Journal of Solar Energy Engineering, 2014. **136**(1): p. 011018-1-011018-8.
3. Wlezien, R., et al., *The Aircraft Morphing Program*, in *39th AIAA/ASME/ASCE/AHS/ASC Structures, Structural Dynamics, and Materials Conference and Exhibit*. 1998: Long Beach, CA. p. 176-187.
4. Ajaj, R.M., et al., *Recent developments in the aeroelasticity of morphing aircraft.* Progress in Aerospace Sciences, 2021. **120**: p. 100682.
5. Barbarino, S., et al., *A Review of Morphing Aircraft.* Journal of Intelligent Material Systems and Structures, 2011. **22**(9): p. 823-877.
6. Montgomery, Z.S., D.F. Hunsaker, and J.J. Joo, *A Methodology for Roll Control of Morphing Aircraft*, in *AIAA Scitech 2019 Forum*.
7. Wu, Z., et al., *Modified adaptive neural dynamic surface control for morphing aircraft with input and output constraints.* Nonlinear Dynamics, 2017. **87**(4): p. 2367-2383.

https://doi.org/10.5194/wes-2022-81
Preprint. Discussion started: 14 October 2022

8. Yan, B., et al., *Adaptive super-twisting sliding mode control of variable sweep morphing aircraft.* Aerospace Science and Technology, 2019. **92**: p. 198-210.
9. Riemenschneider, J., et al. *Chord Morphing for Helicopter Rotor Blades*. in *ASME 2019 Conference on Smart Materials, Adaptive Structures and Intelligent Systems*. 2019.
10. Sal, F., *Effects of the actively morphing root chord and taper on helicopter energy.* Aircraft Engineering and Aerospace Technology, 2020. **92**(2): p. 264-270.
11. Sal, F., *Analysis of combined passively and actively morphing blade root chord length and blade taper for helicopter control.* Aircraft Engineering and Aerospace Technology, 2020. **92**(2): p. 172-179.
12. Vidyarthi, K., et al. *Hoplite - a conceptual design environment for helicopters incorporating morphing rotor technology*. 2018.
13. Abdulrahim, M., H. Garcia, and R. Lind, *Flight Testing a Micro Air Vehicle Using Morphing for Aeroservoelastic Control*, in *45th AIAA/ASME/ASCE/AHS/ASC Structures, Structural Dynamics & Materials Conference*.
14. Abdulrahim, M. and R. Lind. *Modeling and control of micro air vehicles with biologically-inspired morphing*. in *2006 American Control Conference*. 2006.
15. Bilgen, O., et al., *Morphing Wing Micro-Air-Vehicles via Macro-Fiber-Composite Actuators*, in *48th AIAA/ASME/ASCE/AHS/ASC Structures, Structural Dynamics, and Materials Conference*.
16. Garcia, H., M. Abdulrahim, and R. Lind, *Roll Control for a Micro Air Vehicle Using Active Wing Morphing*, in *AIAA Guidance, Navigation, and Control Conference and Exhibit*.
17. Siddall, R., A. Ortega Ancel, and M. Kovač, *Wind and water tunnel testing of a morphing aquatic micro air vehicle.* Interface Focus, 2017. **7**(1): p. 20160085.
18. Gomez, J.C. and E. Garcia, *Morphing unmanned aerial vehicles.* Smart Materials and Structures, 2011. **20**(10): p. 103001.
19. Mir, I., et al., *Optimal morphing – augmented dynamic soaring maneuvers for unmanned air vehicle capable of span and sweep morphologies.* Aerospace Science and Technology, 2018. **79**: p. 17-36.
20. Thangeswaran, R.S.K., et al., *Aerodynamic benefits of flexible morphing airfoil for SUAV.* AIP Conference Proceedings, 2019. **2134**(1): p. 020002.
21. Valasek, J., et al., *Improved Adaptive–Reinforcement Learning Control for Morphing Unmanned Air Vehicles.* IEEE Transactions on Systems, Man, and Cybernetics, Part B (Cybernetics), 2008. **38**(4): p. 1014-1020.
22. Beyene, A. and J. Peffley. *A Morphing Blade for Wave and Wind Energy Conversion*. in *OCEANS 2007 - Europe*. 2007.
23. Barlas, T.K. and G.A.M. van Kuik, *Review of state of the art in smart rotor control research for wind turbines.* Progress in Aerospace Sciences, 2010. **46**(1): p. 1-27.
24. Daynes, S. and P.M. Weaver, *A morphing trailing edge device for a wind turbine.* Journal of Intelligent Material Systems and Structures, 2012. **23**(6): p. 691-701.
25. Ferreira, C.S., et al., *Visualization by PIV of dynamic stall on a vertical axis wind turbine.* Exp Fluids, 2009. **46**(1): p. 97-108.
26. Johnson, S., C. Dam, and D. Berg, *Active Load Control Techniques for Wind Turbines.* 2008.
27. Lachenal, X., S. Daynes, and P.M. Weaver, *Review of morphing concepts and materials for wind turbine blade applications.* Wind Energy, 2013. **16**: p. 283.
28. Lachenal, X., S. Daynes, and P.M. Weaver, *A zero torsional stiffness twist morphing blade as a wind turbine load alleviation device.* Smart Materials and Structures, 2013. **22**(6): p. 065016.
29. MacPhee, D.W. and A. Beyene, *Experimental and Fluid Structure Interaction analysis of a morphing wind turbine rotor.* Energy, 2015. **90**: p. 1055-1065.
30. Rathod, A., et al., *Aerodynamic analysis of morphing blade for horizontal axis wind turbine.* International Journal of Mechanical Engineering and Technology, 2017. **8**: p. 37-44.
31. van Wingerden, J.W., et al., *On the proof of concept of a 'Smart' wind turbine rotor blade for load alleviation.* Wind Energy, 2008. **11**(3): p. 265-280.
32. Wang, W., et al. *Optimal Design of a Simplified Morphing Blade for Fixed-Speed Horizontal Axis Wind Turbines*. in *ASME 2012 International Design Engineering Technical Conferences and Computers and Information in Engineering Conference*. 2012.
33. Zhuang, C., et al., *Effect of morphed trailing-edge flap on aerodynamic load control for a wind turbine blade section.* Renewable Energy, 2020. **148**: p. 964-974.
34. Hand, B., G. Kelly, and A. Cashman, *Numerical simulation of a vertical axis wind turbine airfoil experiencing dynamic stall at high Reynolds numbers.* Comput Fluids, 2017. **149**: p. 12-30.
35. Mulleners, K. and M. Raffel, *The onset of dynamic stall revisited.* Exp Fluids, 2012. **52**(3): p. 779-793.
36. Rezaeiha, A., H. Montazeri, and B. Blocken, *CFD analysis of dynamic stall on vertical axis wind turbines using Scale-Adaptive simulation (SAS): Comparison against URANS and hybrid RANS/LES.* Energy Convers. Manag., 2019. **196**: p. 1282-1298.
37. Rezaeiha, A., H. Montazeri, and B. Blocken, *CFD investigation of separation control on a vertical axis wind turbine: Steady and unsteady suction.* Journal of Physics: Conference Series, 2020. **1618**: p. 052019.
38. E.Amet, et al., *2D Numerical Simulations of Blade-Vortex Interaction in a Darrieus Turbine.* Journal of Fluids Engineering, 2009. **131**: p. (111103)1-15.

39. Tirandaz, M.R. and A. Rezaeiha, *Effect of airfoil shape on power performance of vertical axis wind turbines in dynamic stall: Symmetric Airfoils.* Renewable Energy, 2021. **173**: p. 422-441.
40. Rezaeiha, A., H. Montazeri, and B. Blocken, *A framework for preliminary large-scale urban wind energy potential assessment: Roof-mounted wind turbines.* Energy Conversion and Management, 2020. **214**(C): p. 112770.
41. Sahebzadeh, S., A. Rezaeiha, and H. Montazeri, *Towards optimal layout design of vertical-axis wind-turbine farms: Double rotor arrangements.* Energy Conversion and Management, 2020. **226**(C): p. 113527.
42. Song, C., et al., *Study on aerodynamic characteristics of Darrieus vertical axis wind turbines with different airfoil maximum thicknesses through computational fluid dynamics.* Arab. J. Sci. Eng., 2020. **45**(2): p. 689-698.
43. Jain, S. and U.K. Saha, *On the influence of blade thickness-to-chord ratio on dynamic stall phenomenon in H-type Darrieus wind rotors.* Energy Convers. Manag., 2020. **218**: p. 113024.
44. Nguyen, C.-C. and P.-T. Tran, *A numerical study of thickness effect of the symmetric NACA 4-digit airfoils on self starting capability of a 1kW H-type vertical axis wind turbine.* IJMEA, 2015. **3**(3): p. 7-16.
45. Subramanian, A., et al., *Effect of airfoil and solidity on performance of small scale vertical axis wind turbine using three dimensional CFD model.* Energy, 2017. **133**: p. 179-190.
46. Mazarbhuiya, H.M.S.M., A. Biswas, and K.K. Sharma, *Blade thickness effect on the aerodynamic performance of an asymmetric NACA six series blade vertical axis wind turbine in low wind speed.* Int. J. Green Energy, 2020. **17**(2): p. 171-179.
47. Bedon, G., S. De Betta, and E. Benini, *Performance-optimized airfoil for Darrieus wind turbines.* Renewable Energy, 2016. **94**: p. 328-340.
48. Ma, N., et al., *Airfoil optimization to improve power performance of a high-solidity vertical axis wind turbine at a moderate tip speed ratio.* Energy, 2018. **150**: p. 236-252.
49. Ismail, M.F. and K. Vijayaraghavan, *The effects of aerofoil profile modification on a vertical axis wind turbine performance.* Energy, 2015. **80**: p. 20-31.
50. Tan, J. and M. Paraschivoiu, *CFD-based Performance Analysis of Morphing Aileron for Vertical Axis Wind Turbines*, in *35th AIAA Applied Aerodynamics Conference*.
51. Pechlivanoglou, G., et al., *Active Aerodynamic Control of Wind Turbine Blades with High Deflection Flexible Flaps*, in *48th AIAA Aerospace Sciences Meeting Including the New Horizons Forum and Aerospace Exposition*.
52. Wolff, T., B. Ernst, and J.R. Seume, *Aerodynamic behavior of an airfoil with morphing trailing edge for wind turbine applications.* Journal of Physics: Conference Series, 2014. **524**: p. 012018.
53. Leonczuk Minetto, R.A. and M. Paraschivoiu, *Simulation based analysis of morphing blades applied to a vertical axis wind turbine.* Energy, 2020. **202**: p. 117705.
54. Tescione, G., et al., *Near wake flow analysis of a vertical axis wind turbine by stereoscopic particle image velocimetry.* Renewable Energy, 2014. **70**: p. 47-61.
55. Rezaeiha, A., et al., *Effect of the shaft on the aerodynamic performance of urban vertical axis wind turbines.* Energy Convers. Manag., 2017. **149**: p. 616-630.
56. Rezaeiha, A., H. Montazeri, and B. Blocken, *Towards optimal aerodynamic design of vertical axis wind turbines: Impact of solidity and number of blades.* Energy, 2018. **165**: p. 1129-1148.
57. Rezaeiha, A., H. Montazeri, and B. Blocken, *Characterization of aerodynamic performance of vertical axis wind turbines: impact of operational parameters.* Energy Convers. Manag., 2018. **169**: p. 45-77.
58. Rezaeiha, A., H. Montazeri, and B. Blocken, *CFD analysis of dynamic stall on vertical axis wind turbines using Scale-Adaptive Simulation (SAS): Comparison against URANS and hybrid RANS/LES.* Energy Conversion and Management, 2019. **196**: p. 1282-1298.
59. Rezaeiha, A., H. Montazeri, and B. Blocken, *On the accuracy of turbulence models for CFD simulations of vertical axis wind turbines.* Energy, 2019. **180**: p. 838-857.
60. Rezaeiha, A., H. Montazeri, and B. Blocken. *Scale-Adaptive Simulation (SAS) of Dynamic Stall on a Wind Turbine*. 2020. Cham: Springer International Publishing.
61. Rezaeiha, A., H. Montazeri, and B. Blocken, *Towards accurate CFD simulations of vertical axis wind turbines at different tip speed ratios and solidities: Guidelines for azimuthal increment, domain size and convergence.* Energy Convers. Manag., 2018. **156**: p. 301-316.
62. Rezaeiha, A., H. Montazeri, and B. Blocken, *Active flow control for power enhancement of vertical axis wind turbines: Leading-edge slot suction.* Energy, 2019. **189**: p. 116131.
63. Castelli, M.R., A. Englaro, and E. Benini, *The Darrieus wind turbine: proposal for a new performance prediction model based on CFD.* Energy, 2011. **36**(8): p. 4919-4934.
64. Healy, J., *The influence of blade thickness on the output of vertical axis wind turbines.* Wind Eng., 1978. **2**(1): p. 1-9.
65. McCroskey, W.J., *The phenomenon of dynamic stall*. 1981, National Aeronautics and Space Administration Moffett Field Ca Ames Research ….
66. Sharma, A. and M. Visbal, *Numerical investigation of the effect of airfoil thickness on onset of dynamic stall.* J. Fluid Mech., 2019. **870**: p. 870-900.
67. Frolov, V.A. *Laminar separation point of flow on surface of symmetrical airfoil*. in *AIP Conference Proceedings*. 2016. Perm, Russia: AIP Publishing LLC.

https://doi.org/10.5194/wes-2022-81
Preprint. Discussion started: 14 October 2022

68. Meseguer, J., et al., *On the circulation and the position of the forward stagnation point on airfoils.* Int. J. Mech. Eng. Educ., 2007. **35**(1): p. 65-75.